Individual and cooperative superexchange enhancement in cuprates

Tonghuan Jiang
School of Physics, Peking University, Beijing 100871, P. R. China

Nikolay A. Bogdanov*
Max Planck Institute for Solid State Research, Heisenbergstrasse 1, 70569 Stuttgart, Germany

Ali Alavi†
Max Planck Institute for Solid State Research, Heisenbergstrasse 1, 70569 Stuttgart, Germany and
University of Cambridge, Lensfield Road, Cambridge CB2 1EW, United Kingdom

Ji Chen‡
School of Physics, Peking University, Beijing 100871, P. R. China
Interdisciplinary Institute of Light-Element Quantum Materials and Research Center for Light-Element Advanced Materials, Peking University, Beijing 100871, P. R. China and
Frontiers Science Center for Nano-Optoelectronics, Peking University, Beijing 100871, P. R. China

(Dated: December 1, 2025)

It is now widely accepted that the antiferromagnetic coupling within high temperature superconductors strongly exhibits a profound correlation with the upper limit of superconducting transition temperature these materials can reach. Thus, accurately calculating the positive and negative mechanisms that influence magnetic coupling in specific materials is crucial for the exploration of superconductivity at higher temperatures. Nevertheless, it is notoriously difficult to establish a complete description of electron correlations employing *ab initio* theories because of the large number of orbitals involved. In this study, we tackle the challenge of achieving high-level *ab initio* wave function theory calculations, which allow an explicit treatment of electron correlations associated with a large number of high-energy orbitals. We elucidate the atomic-shell-wise contributions to the superexchange coupling in the lanthanum cuprate, including individual effects of high-energy orbitals (Cu 4d, 5d, 4f, 5p) and cooperative effects between the core and these high-energy orbitals. Specifically, the prominent contributions from Cu 4d, 5d, 4f and 5p give rise to a rich collection of previously unexamined superexchange channels. We propose a *p-d-f* model to universally account for the contributions of high-energy orbitals at copper sites. Our calculations and physical rationalizations offer a more robust theoretical foundation for investigating cuprate-type high-temperature superconductors.

Cuprate unconventional superconductors have received widespread attention in fields of condensed matter physics due to their unique role as the first systems displaying superconductivity above liquid nitrogen temperature [1–3]. Despite extensive research and significant progresses in the past four decades, the precise microscopic mechanisms, including material-specific factors, which underlie the superconductivity have not been fully clarified. The general consensus is that the necessary pairing mechanism in unconventional superconductivity is mediated by strong spin fluctuations in the anti-ferromagnetic correlations of these systems, which provide an effective "glue" for pairing. In this regard, the very large observed superexchange interaction of cuprate materials is highly relevant, and understanding the factors which leads to unusually large superexchange is an important question. Ab initio calculations based on wavefunction methods can play a key role in this regard, partly because they are material-specific, and partly because the description of electronic correlations can systematically controlled and analysed at various levels of theory. This allows both predictive calculations on real systems, as well as obtaining insights into competing effects which give rise to the superexchange, which are very difficult to obtain otherwise [4–13].

Cuprates crystals are formed of copper-oxygen CuO_2 planes and an intercalated ionic bath (Fig. 1a), which serves mainly as charge reservoirs. In undoped CuO_2 planes, Cu and O formally have $+2$ and -2 valence, respectively. Each Cu^{2+} has a $3d^9$ configuration, with one hole occupying the $3d_{x^2-y^2}$ orbital to form a spin-1/2 site, forming an antiferromagnetic (AFM) ground state (Fig. 1b)[1, 2]. In the doped case, long-range AFM order breaks down quickly, yet the extra charges from the ion bath lead to Cooper pair formation in CuO_2 planes, in which spin-fluctuations are nevertheless believed to play a key role. [1–3]. Recently Wang et al. proposed an empirical linear dependence between critical temperature (T_c) and AFM coupling in a family of Hg-based cuprates, where a 1 meV enhancement of AFM coupling is accompanied by several Kelvins of T_c increase [14].

* n.bogdanov@fkf.mpg.de
† a.alavi@fkf.mpg.de
‡ ji.chen@pku.edu.cn

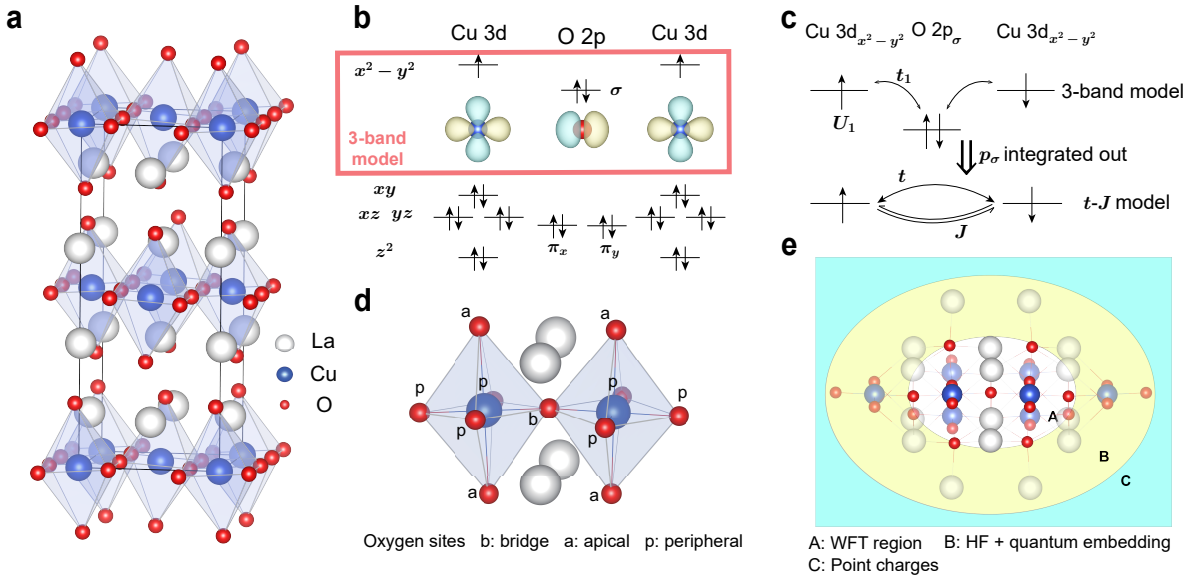

FIG. 1. Computational and theoretical models. (a) Crystal structure of La_2CuO_4. (b) Key aspects of the electronic structure of cuprates. The leading electron configuration of parent compound's ground state is shown, where Cu^{2+} and O^{2-} have $3d^9$ and O^{2-} $2p^6$ configurations, respectively. The pink box highlights the orbitals considered in the 3-band model. (c) Effective low-energy models derived on key orbitals in cuprates, i.e., Cu $3d_{x^2-y^2}$ and O $2p_\sigma$, including the 3-band model and the t-J model. (d) The $Cu_2O_{11}La_4$ cluster containing two nearest-neighbor Cu sites and 3 types of oxygen (bridge, apical and peripheral). (e) The three-layer embedding scheme adopted in this work. The correlated WFT calculations are performed on the $Cu_2O_{11}La_4$ cluster (A, white background), and the environment is split into two layers: the inner quantum projection embedding part (B, yellow shade), and the outer classical point-charge embedding part (C, cyan shade).

The empirical linear relationship has been further supported by the theoretical work of Qin et al. [15], which demonstrated that the maximum superconducting transition temperature (T_c) of unconventional superconductors cannot exceed 0.04 to 0.07 times the pairing interaction strength. Given the correlation between exchange interaction J and the upper limit of T_c, in the pursuit of higher temperature superconducting materials, it is of utmost importance to accurately compute, with meV-precision, the mechanisms that either enhance or impede J.

In recent years, *ab initio* wave function theories (WFT) have been developed rapidly, providing new opportunities to accurately tackle complex materials with strong electron correlations [16–23]. Such calculations are used to obtain quantitatively accurate descriptions, to check the validity of existing models of cuprates, and to provide better theoretical models to fit experimental measurements [6, 7, 24–30]. The calculations on cuprate superconductivity ($T_c \sim 40$ K) usually require a meV accuracy on their magnetic coupling in their undoped phase, rather than traditional chemical accuracy (1 kcal/mol $\approx$ 500 K) [1, 2]. Effective models of cuprates, such as the 3-band Hubbard model and the t-J model, consider effective renormalized interactions within Cu $3d_{x^2-y^2}$ and O $2p_\sigma$ orbitals (Fig. 1c) [1, 31]. Some studies would include Cu 4s and O $2p_z$ orbitals, but recent WFT analyses suggested a more complex picture, such that simplifications could lead to a severe underestimation of the AFM superexchange, highlighting an essential role of both static and dynamic correlations from high-energy bands [2, 6, 24, 25, 27, 32, 33]. For instance, a new superexchange channel due to orbital breathing within the Cu d shell can bring J up to one half of the experimental value in Sr_2CuO_3 and two thirds in La_2CuO_4 [6]. However, a considerable portion of J ($\approx 35\%$ in La_2CuO_4, and $\approx 48\%$ in Sr_2CuO_3) remains unexplained, indicating the existence of uncovered channels in superexchange. Moreover, it is desirable to scrutinize the real interactions behind the simplified effective models and parameters.

In this work, we devise a computational framework utilizing three-layer quantum embedding and high-level WFT to achieve an accurate *ab initio* calculation of the nearest-neighbor AFM coupling in the prototypical cuprate parent compound, La_2CuO_4. Specifically, a $Cu_2O_{11}La_4$ cluster (Fig. 1d) is selected out of the La_2CuO_4 crystal for correlated WFT computations. The embedding scheme is illustrated in Fig. 1e. The $Cu_2O_{11}La_4$ cluster (A) is surrounded by a 2-layer environment, the quantum projection embedding (B) [34] and classical point charge bath (C) , which describe the short-range and long-range environment interaction, respectively. A new spin-averaged Hartree-Fock scheme is designed to describe the antiferromagnetic environment within the mean-field level. The WFT methods used include complete active space self-consistent field

(CASSCF) [35], full-configuration interaction quantum Monte Carlo (FCIQMC) [16, 36], the density matrix renormalization group (DMRG) [17, 18] and the strongly contracted second-order n-electron valence state perturbation theory (SC-NEVPT2) [19, 20, 37]. See the *Methods* Section for further computational details.

In order to determine the AFM coupling J, we perform a calculation of states of different spin multiplicity within the cluster containing two magnetic centers [38]. J is calculated by the energy difference between the lowest spin-singlet state and the lowest spin-triplet state. This method was successfully applied to compute magnetic couplings in various transition-metal oxides [6, 25, 26, 39, 40]. The use of WFT methods allowed us to systematically examine the atomic-orbital characters of the AFM coupling. This is done by computing J including different sets of high-energy atomic orbitals in the correlated WFT calculations, and comparing their contribution. We find that the contribution of high-energy orbitals includes two parts, the *individual* effect and the *cooperative* effect, both having prominent impacts on AFM coupling of cuprates. Within the high-energy orbitals, Cu 4d, 5d, 4f and 5p were found to contribute the most. Based on the *ab initio* results, we establish a theoretical model to describe the previously unexplored superexchange mechanisms in cuprates.

RESULTS

Superexchange enhancement

Previous *ab initio* works have already demonstrated the possibility of superexchange enhancement due to electron correlation effects [6, 25, 28]. These works pointed to the collective effects of large numbers of high-energy orbitals, often referred to as dynamic correlations [41]. Here, in order to lay a solid foundation for further discussion on orbital contributions, it is necessary to revisit and clarify the concept of superexchange enhancement using different orbital settings to calculate J. To achieve reliable conclusions, we have employed various wave function methods, the results are summarized in Table I.

First, CASSCF calculations were performed on a small active space, CAS(4e,3o), including only the essential orbitals that correspond the 3-band Hubbard model, i.e. Cu $3d_{x^2-y^2}$ and bridging O $2p_\sigma$. Magnetic coupling obtained from these calculations turns out to be only $J = 35.5$ meV. In line with previous studies, such a calculation results in a significant underestimate of superexchange fitted from experimental measurements, which is ≈ 138 meV[6, 42, 43]. When the entire Cu 3d, 4d and the bridging O 2p, 3p shells are included in the active space, forming CAS(24e,26o), J is enhanced to 92.2 meV or 92.9 meV using DMRG or FCIQMC solvers respectively. These results further support the *orbital breathing* effect, in which the spatial expansion of the effective Cu 3d orbitals due to the correlation with Cu 4d increases the effective *dd*-hopping (t) and reduces on-site Coulomb repulsion (U), eventually enhancing $J \approx 4t^2/U$ [6].

Although the *orbital breathing* captures the leading contribution, the calculated J is still 30 - 50 meV away from the reference values [42, 43]. Once we consider the effect of the whole orbital space using NEVPT2 on top of the CAS(24e,26o) reference wave function, we find that J increases to 143.8 meV, which is close to the experiment value, manifesting the significant enhancement due to correlations with higher-energy orbitals [6, 42, 43].

To further support the validity of embedding treatment, we demonstrate the weak influence of the environment by excluding the empty orbitals of region B from the perturbation space. Since all the occupied orbitals in region B have been projected out in the embedding scheme [34], the remaining environment orbital space consists of only B virtual orbitals. The exclusion of B virtual orbitals reduces the number of the correlated virtual orbitals from 368 to 180, yet AFM J is decreased by only 2 meV (143.8 meV to 141.7 meV). The result containing correlation effects of environment empty orbitals is also consistent with the literature where the environment is treated with classical Coulomb potential of point charges and effective core potentials (ECP) [6, 25, 26]. This confirms that the environment effects on AFM coupling are negligible.

Having reproduced all the known correlation effects for superexchange enhancement in cuprates, we are ready to further disentangle the contributions of core and virtual orbitals. We can conceptually divide the correlation effects of the core and virtual orbitals into three parts (Fig. 2a). (i) The part that only involves the virtual orbitals and is unrelated to the core. This refers to the contribution resulting from the correlation of active electrons in virtual orbitals, abbreviated as "individual virtual contribution" (IVC). It is mainly related to the excitation of active electrons to specific virtual orbitals, such as intersite hopping paths or radial diffusion of Cu 3d electrons. (ii) The part that only involves the core orbitals and is

TABLE I. AFM coupling J with different WFT calculations. "PT" stands for "perturbation". The (mc,nv) in "PT size" column means that m core orbitals and n virtual orbitals are correlated in NEVPT2 calculations. Experimental values are taken from spin wave measurements. The "ED" refers to exact diagonalization using Davidson algorithm as the eigenvalue solver.

CAS size	CAS solver	PT space	PT size	J (meV)
(4e,3o)	ED	None	None	35.51
(24e,26o)	DMRG	None	None	92.24
(24e,26o)	FCIQMC	None	None	92.9(8)
(24e,26o)	DMRG	Full WFT space	(86c,368v)	143.78
(24e,26o)	DMRG	Frozen env	(86c,180v)	141.73
(24e,26o)	DMRG	Frozen core	(0c,180v)	123.74
(24e,26o)	DMRG	Frozen virt	(86c,0v)	91.82
			Exp.	120 [42]
				138 [43]

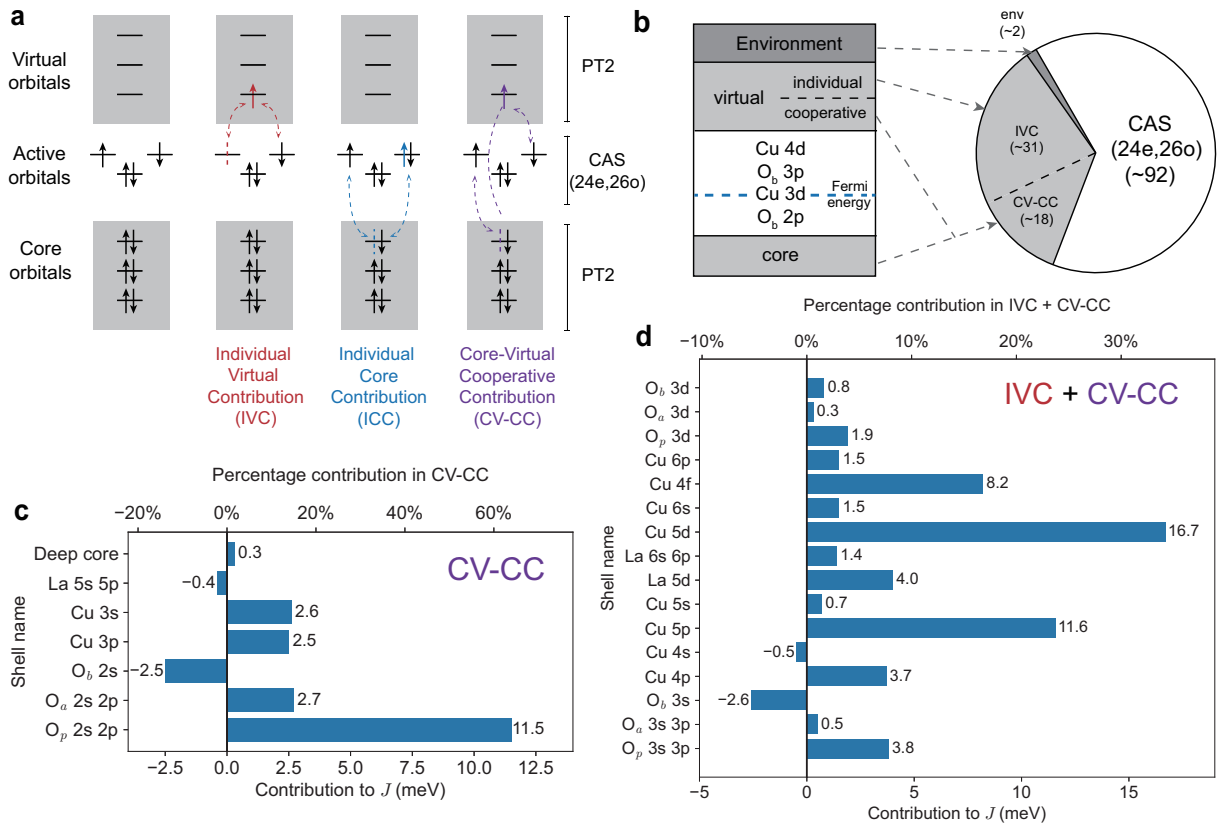

FIG. 2. Diagrams displaying atomic-shell-wise contributions to superexchange enhancement. (a) Scheme showing different contributions. Orbital contributions beyond CAS can be divided into 3 parts according to the nature of their electronic configuration: ICC, where electrons are excited from core shells to active space; IVC, where electrons are excited from active space to virtual shells; and CV-CC, where both core excitations and virtual excitations occur. (b) The weight of different sources of AFM enhancement shown as a pie chart. The multi-reference CAS wave function involving Cu 3d, 4d, and bridging O 2p, 3p adds ∼92 meV to AFM coupling. The remaining substantial orbitals contributions are IVC (∼31 meV) and CV-CC (∼18 meV), while ICC (< 1 meV) and environment orbitals beyond Cu_2O_7 unit (4 ∼ 2 meV) are negligible. (c) The contribution of different core shells to CV-CC. "Deep core" denotes atomic shells Cu 1s, Cu 2s, Cu 2p and O 1s. The combined contribution of all core shells equals CV-CC (18.0 meV) and is set as 100%. The summed contribution of all non-intersecting core shells is 16.7 meV. (d) The contribution of different virtual shells to IVC and CV-CC. The perturbation space in core orbitals is fixed to the Core-CuO space (see the main text for details). The combined contribution equals IVC + CV-CC (48.8 meV) and is set as 100%. The summed contribution of all non-intersecting virtual shells is 53.5 meV. The reference space ($\mathcal{B}$) for atomic shell contributions shown in (c) and (d) is discussed in SI Section I.

unrelated to the virtual orbitals. This defines the correlation between core and active electrons, abbreviated as "individual core contribution" (ICC), and is mainly related to hole excitations from active space to core orbitals. (iii) The part that involves core and virtual orbitals simultaneously, abbreviated as "core-virtual cooperative contribution" (CV-CC).

Let us define AFM J from CAS(24e,26o) be $J_{\mathrm{CAS}} = 92.2$ meV, and IVC, ICC, and CV-CC to AFM J be Δ_{IVC}, Δ_{ICC}, and $\Delta_{\text{CV-CC}}$, respectively. Then J correlating different PT orbital sets can be written as

$$\begin{aligned} J_{\mathrm{v}} &= J_{\mathrm{CAS}} + \Delta_{\mathrm{IVC}}, \\ J_{\mathrm{c}} &= J_{\mathrm{CAS}} + \Delta_{\mathrm{ICC}}, \\ J_{\mathrm{cv}} &= J_{\mathrm{CAS}} + \Delta_{\mathrm{ICC}} + \Delta_{\mathrm{IVC}} + \Delta_{\text{CV-CC}}, \end{aligned} \tag{1}$$

where $J_{\mathrm{c}}, J_{\mathrm{v}}, J_{\mathrm{cv}}$ denote AFM J obtained in three different perturbation settings respectively: core space only (J_{c}), virtual space only (J_{v}), and core and virtual both (J_{cv}). In other words, CV-CC represents the part of the correlation effect that arises only when both core and virtual correlations are present.

To evaluate sources of different contributions, NEVPT2 calculations on top of the CAS(24e,26o) reference are conducted with different perturbation space selections. We observe that removing virtual orbitals from the perturbation treatment causes J to fall from $J_{\mathrm{cv}} = 141.7$ meV to $J_{\mathrm{c}} = 91.8$ meV, while removing core orbitals leads to a much smaller reduction, $J_{\mathrm{v}} = 123.7$ meV. In this way, one can see that the correlation effects consist mainly from two parts, IVC (∼ 31 meV) and CV-CC (∼ 18 meV). The individual core contribution, ICC, is in fact negligible

($|\Delta_{\mathrm{ICC}}| < 1$ meV). Hence, core orbitals only have an influence on J when treated together with virtual orbitals, while virtual orbitals lead to an enhancement of J by ~ 31 meV even when they are present alone (Fig. 2b).

In this subsection, we have considered orbitals outside the CAS(24e,26o) space, investigating the effects of both the cluster's additional orbitals and the environmental orbitals on the AFM coupling between the Cu sites. Furthermore, the core and virtual orbitals within the cluster can be subdivided into separate atomic shells. In the next two subsections, we will further elucidate the contributions from these atomic shells, identify the crucial shells, and thereby uncover potential new superexchange pathways.

Atomic-shell-wise correlation effects

First, we discuss how each core and virtual shell contribute to superexchange (Fig. 2c-d), and identify the shells having significant impact on AFM J. The contribution of a set of core orbitals X can be evaluated by comparing the AFM coupling calculation *with* and *without* X included in the correlation treatment.

$$\Delta_{\mathcal{B}}[X] = J[\mathcal{B}] - J[\mathcal{B} \setminus X] \tag{2}$$

where the contribution of X, $\Delta_{\mathcal{B}}[X]$, is the difference of J brought by the inclusion of X in the correlated WFT solver, with $\mathcal{B}$ being the corresponding reference space. This way, the contribution of X depends on the reference space $\mathcal{B}$. Therefore, to ensure the validity of comparison, the contributions of different shells are calculated using the same reference space. More detailed description of reference space selection can be seen in SI Section I. After calculating the contribution of several atomic shells $\{X_1, ..., X_N\}$, we also check the difference between the summed contribution $\sum_{i=1}^{N} \Delta_{\mathcal{B}}[X_i]$ and the combined one $\Delta_{\mathcal{B}}\left[\bigcup_{i=1}^{N} X_i\right]$. This difference denotes the non-additive cooperative effects between the selected shells $\{X_1, ..., X_N\}$. As discussed in the previous section, significant core contributions occur only if both core and virtual shells are correlated, therefore the core contributions listed below belong to CV-CC.

The contributions of each core atomic shell are shown in Fig. 2c. Core orbital contribution to J are mainly concentrated in a set of shallow orbitals, termed "Core-CuO", which consists of Cu 3s, 3p, O_b 2s and $O_{(a,p)}$ 2s, 2p. The subscript in $O_{(b,a,p)}$ denotes the bridging, apical and peripheral oxygens, respectively, as illustrated in Fig. 1d. The rest of core orbitals, i.e. deep-core orbitals (O K, Cu K and L shells), and La orbitals (5s 5p), all exhibit very small contributions to J, less than 0.7 meV in total. Therefore, Core-CuO encompasses the dominant electron correlation effects within the core shell, and thus is used as the perturbative core space in subsequent calculations on virtual shells. Among all the core orbital contributions, the peripheral O 2s and 2p shells are the most important ones, contributing 11.5 meV. We also find that this contribution can be further divided into two parts: 5.8 meV individual effect of 2p, and 5.3 meV cooperative effect between 2s and 2p. Note that the found cooperative effect is a justification for the well known O 2p-Cu 3d correlation. It is also worth mentioning that the cooperative effects within core shells, measured by the difference between the combined and the summed contributions (Fig. 2c), is negligible (1.3 meV). This ensures the validity of discussion about the individual contributions of each atomic orbital shell.

TABLE II. The cooperative effects ($\Delta^{\text{coop.}}[\mathcal{C}, X]$) between core and virtual orbitals, evaluated as the difference between calculations with and without core. $\mathcal{C}$ stands for "Core-CuO" described in the text. Details of the reference PT space are presented in Tables SI and SV in the SI.

virtual shell X	with core $\Delta_{\mathcal{C}}[X]$	w/o core $\Delta[X]$	$\Delta^{\text{coop.}}[\mathcal{C}, X]$
Cu 4f 5p 5d	34.6	35.5	−0.8
O_b 3s O_p 3s 3p Cu 4p	2.5	2.4	0.1
La 5d	4.1	0.8	3.3
Cu 4s 5s	−0.1	0.3	−0.5
O_a 3s 3p	0.5	0.2	0.3
La 6s 6p	1.5	0.3	1.2
Cu 6s 6p	3.1	0.2	2.9
O_b 3d	0.6	−8.6	9.1
$O_{(a,p)}$ 3d	2.1	0.5	1.6
Total	48.8	31.5	17.3

The contributions of virtual atomic shells are investigated the same way, with the only difference being that virtual orbitals are subject to both IVC and CV-CC (Fig. 2d). The perturbative core space is set to Core-CuO, such that both the individual and the cooperative virtual orbitals contributions are included. Interestingly, unlike the core space, high-energy orbitals in the virtual space do make important contributions. For example, the largest contributions of virtual orbitals come from high-energy shells, namely from Cu 5d (16.7 meV), Cu 5p (11.6 meV), and Cu 4f (8.2 meV) orbitals. These shells together make up approximately 70% of the remaining unexplained AFM coupling. The effect of Cu 5d is the *orbital breathing*, similar to the effect of Cu 4d. These high-energy Cu d orbitals are relatively diffuse, promoting hopping between neighboring sites (increasing t) and weakening the on-site repulsion of effective 3d orbitals (reducing U). Strikingly, our calculations indicate that orbitals with other symmetries, namely Cu 4f and 5p, also contribute to the AFM coupling enhancement. This will be discussed later in the subsection .

Cooperative effects between core and virtual orbitals

Once we have identified core and virtual shells crucial for exchange, we can further differentiate the individual effects of virtual shells (IVC) from the cooperative effects between core and virtual shells (CV-CC) establishing the basis for an integrated theoretical picture of AFM exchange. To achieve this, we calculate the contribution of each virtual shell X with and without core orbitals ($\mathcal{C}$) being correlated, denoted as $\Delta_{\mathcal{B}\cup\mathcal{C}}[X]$ and $\Delta_{\mathcal{B}}[X]$, respectively. The cooperative effect between core shell $\mathcal{C}$ and a virtual shell X, referred to as $\Delta_{\mathcal{B}}^{\text{coop.}}[\mathcal{C},X] = \Delta_{\mathcal{B}\cup\mathcal{C}}[X] - \Delta_{\mathcal{B}}[X]$, is listed in Table II. One can observe that the virtual shells Cu 4f, 5p, and 5d do not exhibit cooperative effects with the core, despite their large individual effects on J. The shells with significant cooperative effects are oxygen 3d and highly-diffuse orbitals, e.g. Cu 6s 6p, La 5d 6s 6p. Although perturbation theory usually suggests that orbitals with higher energies play less important role in low-energy physics, our calculations demonstrate that their contributions are not trivial.

In particular, the contribution of bridging oxygen 3d orbitals (O_b 3d) to AFM coupling shows a peculiar feature. Without the correlation of core orbitals, the inclusion of O_b 3d results in a significant reduction of J (-8.6 meV), indicating that the inclusion of O_b 3d alone introduces an extra hopping pathway between nearest-neighbor copper sites. Due to the even parity of O 3d orbitals, the contribution from this two-step hopping has the opposite sign compared to the original *dd*-hopping, thereby weakening AFM coupling. However, with the core orbitals correlated, the aforementioned weakening of AFM coupling is counterbalanced.

Computational results of two subsections above are summarized in a schematic diagram presented in Fig. 2b, illustrating the contributions of various atomic orbitals to the AFM coupling. This includes a ~ 92 meV contribution from CAS(24e,26o), ~ 31 meV from the individual contributions of virtual orbitals, $\sim$18 meV from the cooperative contributions between virtual and core orbitals, and approximately ~ 2 meV from the environmental effects. Within the individual contributions of virtual orbitals, the prominent correlation effects from Cu high-energy orbitals (4f, 5d and 5p) are found, demonstrating their relevance for the exchange process. Among the cooperative contributions between virtual and core orbitals, most significant effects arise from virtual La, high-energy Cu (6s, 6p), and O 3d orbitals.

Extended theoretical models for cuprates

Following numerical evidence of prominent contributions of high-energy orbitals, it is instructive to establish an effective model beyond minimal that can faithfully capture elemental exchange mechanisms behind the large AFM coupling in cuprates, providing new foundations to study their emergent physics. We start with the *orbital breathing* model [6] proposed for Cu 4d, but also valid for Cu 5d, where the on-site exchange integrals serve as a driving force, formulated as

$$K = \int d\mathbf{r}_1 d\mathbf{r}_2 \frac{\phi^*_{3d}(\mathbf{r}_1)\phi_{3d}(\mathbf{r}_1)\phi^*_{3d}(\mathbf{r}_2)\phi_{5d}(\mathbf{r}_2)}{|\mathbf{r}_1 - \mathbf{r}_2|}. \quad (3)$$

The correlation of diffuse Cu d orbitals promotes the effective *dd*-hopping and reduces the on-site Coulomb repulsion, and thus enhances J. However, a substitution of 5d orbital with 4f or 5p in the integral above yields a vanishing K due to the odd parity of 4f or 5p orbitals. Therefore, the contribution coming from Cu 4f and 5p cannot be explained within the orbital breathing mechanism. To this end, we propose a further extension of the effective model, termed "*p-d-f* model".

The 2-site *p-d-f* model contains 3 types of orbitals, Cu $3d_{x^2-y^2}$ (d), O $2p_\sigma$ (p), and an additional orbital which can be either Cu 4f or 5p, denoted as f (see Fig. 3). The Hamiltonian then includes terms corresponding to the integrals found to be important in *ab initio* calculations. Those are on-site (U_p, U_d) and nearest-neighbor U_{pd} Coulomb repulsion terms, nearest-neighbor hoppings t_{pd}, t_{pf} and t_{dd}, and exchange integrals K_{pd} and K_{df}. K_{df} (colored in blue in Fig. 3) and t_{pf} (colored in red in Fig. 3) are the only two integrals that involve interaction with high-energy f-levels. They represent two different superexchange channels that play important role for Cu 4f and 5p contributions, respectively, termed as "*df* angular exchange" and "*pf* direct hopping". The integrals

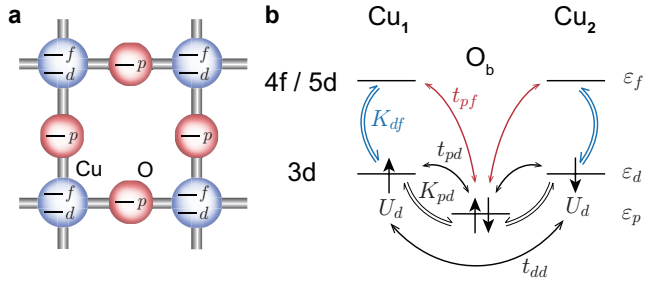

FIG. 3. Diagram of the *p-d-f* model showing Cu 4f and 5p contributions to AFM coupling. (a) The periodic version of 4-band *p-d-f* model. Each Cu^{2+} ion contains a $3d_{x^2-y^2}$ orbital (labelled as d) and another high-energy orbital which can be either 4f or 5p (labelled as f). Each O^{2-} ion has its $2p_\sigma$ labelled as p. (b) The 2-site local version of *p-d-f* model. The 5 orbitals in the model is shown in their energy ordering, along with all the inter-orbital integrals in the model. Among these orbitals, the two integrals involving f-levels, K_{df} (blue) and t_{pf} (red), are the main source of f participation in AFM coupling enhancement. Other integrals belong to a revision of 3-band model with inter-site exchange integrals, K_{pd}, and direct *dd*-hopping, t_{dd}, and a more complicated form of *dp*-hopping (SI Section III).

are defined as follows.

$$K_{df} = \int d\mathbf{r}_1 d\mathbf{r}_2 \frac{\phi_d^*(\mathbf{r}_1)\phi_f(\mathbf{r}_1)\phi_d^*(\mathbf{r}_2)\phi_f(\mathbf{r}_2)}{|\mathbf{r}_1 - \mathbf{r}_2|}$$
$$t_{pf} = \int d\mathbf{r}_1 d\mathbf{r}_2 \phi_p^*(\mathbf{r}_1)\hat{H}_{\text{1-body}}(\mathbf{r}_1, \mathbf{r}_2)\phi_f(\mathbf{r}_2) \tag{4}$$

We can split the Hamiltonian for the 2-site *p-d-f* model into an unperturbed $\hat{H}_0$ and a perturbation $\hat{H}_1$. $\hat{H}_0$ includes orbital energy and Coulomb repulsion terms:

$$\begin{aligned}\hat{H}_0 = \epsilon_d \sum_{L=1}^{2} \hat{n}_{Ld} + \epsilon_p \hat{n}_p + \epsilon_f \sum_{L=1}^{2} \hat{n}_{Lf} + U_d \sum_{L=1}^{2} \hat{n}_{Ld\uparrow}\hat{n}_{Ld\downarrow} \\ + U_{pd} \sum_{L=1}^{2} \hat{n}_{Ld}\hat{n}_p + U_p \hat{n}_{p\uparrow}\hat{n}_{p\downarrow} + U_{dd}\hat{n}_{d1}\hat{n}_{d2}.\end{aligned} \tag{5}$$

Here $\hat{n}_x$ denotes the electron number operator of spatial orbital x, and n_{Ld} and $n_{Ld\uparrow}$ denote the spin-summed and spin-up electron number operator on d orbital of Cu atom L, respectively. The perturbative part $\hat{H}_1$ is formulated as

$$\begin{aligned}\hat{H}_1 = &\Big(\hat{h}_{d1,p}(-t_{pd1}(\hat{n}_{d1} - \frac{1}{2}) + t_{pd2}(\hat{n}_p - \frac{1}{2}) + t_{pd3}\hat{n}_{d2}) \\ &-\hat{h}_{d2,p}(-t_{pd1}(\hat{n}_{d2} - \frac{1}{2}) + t_{pd2}(\hat{n}_p - \frac{1}{2}) + t_{pd3}\hat{n}_{d1})\Big) \\ &+ (h.c.) + t_{pf}(\hat{h}_{f1,p} + \hat{h}_{f2,p}) + t_{dd}\hat{h}_{d1,d2} \\ &+ \frac{1}{2}K_{pd}\sum_{L=1}^{2}\Big(\hat{h}_{dL,p}^2 - \hat{n}_{dL} - \hat{n}_p\Big) \\ &+ \frac{1}{2}K_{df}\sum_{L=1}^{2}\Big(\hat{h}_{dL,fL}^2 - \hat{n}_{dL} - \hat{n}_{fL}\Big),\end{aligned} \tag{6}$$

where $\hat{h}_{xy} = \sum_\sigma (\hat{x}_\sigma^\dagger \hat{y}_\sigma + \hat{y}_\sigma^\dagger \hat{x}_\sigma)$ denotes the hopping between two spatial orbitals x and y. t_{pd1}, t_{pd2} and t_{pd3} denote *dp*-hopping related to different integrals. The values of all parameters can be estimated from the *ab initio* Hamiltonian with only the five orbitals corresponding to the model levels being active. The full table of parameters is presented in SI Table SVI. It turns out that *df* angular exchange channel, represented by K_{df}, plays the dominant role for the Cu 4f contribution to J. For Cu 5p orbitals contribution, however, the *pf* direct hopping surpasses the *df* channel and becomes the leading force. In the following text, the contributions of K_{df} and t_{pf} to AFM J will be considered separately. The rest of the Hamiltonian is a variant of 3-band model, which contains direct *dd* hopping t_{dd} and *dp*-exchange K_{pd}. We perform analysis of the 2-site *p-d-f* model using the downfolding and perturbation method, which are explained in detail in SI Section II.

Setting $|d_{1\uparrow}d_{2\downarrow}p^2\rangle$ and $|d_{1\downarrow}d_{2\uparrow}p^2\rangle$ to be the reference states, one can obtain the effective Hamiltonian on these states, and then the AFM coupling as the spin gap within the effective Hamiltonian. First, we constrain ourselves to the lowest order contribution to AFM coupling, the second-order with respect to (H_1) ($(H_1)^2$-order) perturbation; magnetic coupling obtained this way is denoted as $J^{(2)}$. It resembles the known result $J^{(2)} = 4t_{dd}^2/U_{\text{eff}}$, where U_{eff} is calculated as $U_{\text{eff}} = U_d - U_{dd} = E[d_1^2p^2] - E[d_{1\uparrow}d_{2\downarrow}p^2]$, and does not contain any *f*-level contribution to AFM coupling.

Moving to higher-order perturbations one by one, we find that K_{df} contribution shows up only at the $(H_1)^4(\epsilon_f - \epsilon_d)^{-1}$ order. If we adopt $J^{(m,n)}$ notation for J obtained using the $(H_1)^m(\epsilon_f - \epsilon_d)^{-n}$-order perturbation, the leading contribution of K_{df} to J is $J_K^{(4,1)}$:

$$J_K^{(4,1)} = \frac{2K_{df}^2 t_{dd}^2}{(\epsilon_f - \epsilon_d)U_{\text{eff}}^2}. \tag{7}$$

$J_K^{(4,1)}$ is always positive, which indicates the AFM contribution of Cu 4f to magnetic coupling.

The lowest-order occurrence of t_{pf} is at $(H_1)^4(\epsilon_f - \epsilon_d)^{-2}$ and $(H_1)^5(\epsilon_f - \epsilon_d)^{-1}$ order. The former reads

$$J_t^{(4,2)} = \frac{16t_{pf}^2 t_{dd}^2}{(\epsilon_f - \epsilon_d)^2 U_{\text{eff}}}, \tag{8}$$

while the latter is

$$J_t^{(5,1)} = \frac{16t_{pf}^2 t_2}{(\epsilon_f - \epsilon_d)U_{\text{1CT}}^3}\left(\frac{t_{dd}t_1 U_{\text{1CT}}}{U_{\text{eff}}} + t_{pd2}(K_{pd} - t_{dd})\right), \tag{9}$$

where $U_{\text{1CT}} = \epsilon_d - \epsilon_p + U_d - U_{pd} + U_{dd} + U_p = E[d_1^2 d_{2\downarrow} p_\uparrow] - E[d_{1\uparrow}d_{2\downarrow}p^2]$, $t_1 = \langle d_{1\downarrow}d_2^2 p_\uparrow|\hat{H}|d_2^2p^2\rangle = 2t_{pd3} + t_{pd2}$, and $t_2 = \langle d_{1\downarrow}d_{2\uparrow}p^2|\hat{H}|d_{1\downarrow}d_2^2p_\uparrow\rangle = t_{pd1} - t_{pd2} - t_{pd3}$. Our numerical results show $K_{pd} > t_{dd}$, hence both $J_t^{(4,2)}$ and $J_t^{(5,1)}$ are positive contributions to J. This demonstrates the AFM contribution to J arising from the Cu 5p orbitals.

In summary, based on the extended model, we find the increase of AFM J due to the introduction of Cu 4f and 5p have different sources. Cu 4f orbitals are involved with *df* angular exchange channel of superexchange characterized with K_{df}, which reduces the effective 3d on-site Hubbard repulsion by accepting electron-pair hopping from 3d to 4f. Among the Cu 4f shell, the $x(x^2-y^2)$, $y(x^2-y^2)$ and $z(x^2-y^2)$ components have the largest K_{df} integrals (~ 0.1 E_h) and contribute the most to the *df* angular exchange channel. Cu 5p orbitals, however, do not have such large K_{df} integrals, and participate in AFM coupling via *pf* direct hopping characterized with t_{pf}. The presented *p-d-f* model can be further employed in future theoretical research to encode electron correlations within high-energy bands, improving the low-energy models and our understanding of high-temperature superconductivity.

DISCUSSION

By leveraging accurate correlated WFT calculations, we have comprensensively elucidated the orbtial-resolved contributions to the superexchange mechanism in cuprates. The exceptionally strong AFM coupling prevalent in these materials has been demonstrated to predominantly originate from electronic correlations within the high-energy copper bands. This correlation-driven enhancement comprises three synergistic components: (i) The *radial breathing* effect, manifested in high-energy Cu d orbitals such as 4d and 5d, arises from radial hybridization between Cu 3d orbitals. (ii) The *angular exchange* effect, prominent in Cu 4f orbitals, stems from exchange interactions between d-orbitals and those with distinct angular momentum symmetries; (iii) The *direct hopping* effect, observed in Cu 5p orbitals, emerges from oxygen-mediated hopping processes involving high-energy Cu orbitals. Collectively, these mechanisms magnify the Cu-centered AFM exchange interaction from an unrenormalized value of ~ 35 meV to ~ 127 meV, establishing the microscopic foundation for the extraordinary spin-fluctuation-mediated high-temperature superconductivity.

Our quantitative analysis further elucidates the collective effects of high-energy atomic shells on magnetic coupling. The collective effects can be categorized into individual virtual contributions (IVC, 31 meV), core-virtual cooperative contributions (CV-CC, 18 meV), and environmental contributions (2 meV), according to the orbitals excitations involved. The aforementioned mechanisms driven by copper orbitals primarily operate through individual orbital channels, while cooperative effects are manifested primarily in O 3d orbitals and highly delocalized Cu/La states. These computational insights reveal the atomic-scale origins of dominant electronic correlation effects on magnetic coupling, offering a refined perspective on the physics of cuprates.

Significantly, this work uncovers a more comprehensive picture of high-energy orbital correlation effects on enhancing the nearest neighbor AFM coupling. This achievement not only provides guidance to design appropriate active spaces for subsequent theoretical calculations, but also identifies the physically most crucial channels in superexchange formation. Our study accentuates the significance of high-energy Cu orbitals within the low-energy physics of cuprates, paving the way for improving commonly used theoretical models. The rectification of high-energy copper bands in low-energy models may encompass the following facets: (i) amendments to effective parameters in existing 3-band models; (ii) expansions of the model to incorporate *p-d* bands; (iii) extensions of the model to account for high-energy bands. All these aspects can potentially tailor the model phase diagram behavior in a quantitative or qualitative way. This study also lay a solid foundation to further explore the dynamic correlation effects beyond AFM coupling in cuprates. Resolving the correlation effects on doped states or longer-range magnetic coupling will further advance our understanding of relationship between chemical composition and physical properties of high-temperature superconductors.

METHODS

The crystal structure of La_2CuO_4 is taken from Crystallography Open Database No. 2002183 [44, 45], with an orthorhombic *Abma* symmetry and crystal constants $a = 5.406\text{Å}, b = 5.370\text{Å}, c = 13.15\text{Å}$ (Fig. 1a). In our embedding computation scheme, the La_2CuO_4 crystal is divided into 3 layers (Fig. 1e): core layer (A) ($Cu_2O_{11}La_4$) handled with high-order wave function theories, middle layer (B) ($Cu_6O_{16}La_{12}$) handled with spin-averaged Hartree-Fock, and outermost layer (C) handled as an array of point charges.

Point charge embedding

As the first step of our embedding procedure, an array of point charges located outside of A+B (quantum cluster) is generated to reproduce the electrostatic potential within the quantum cluster with the `chargedel` tool, using the extended Evjen scheme [46, 47]. The $Cu_8O_{27}La_{16}$ quantum cluster is centered at two nearest neighbor copper sites and contains all atoms adjacent to these sites (Fig. 1e). The electrostatic potential within the quantum region is approximated to reproduce the Madelung potential, assuming that La, Cu and O have formal charges of $+3$, $+2$, -2 valence. The point charges are further divided into 2 parts, the normal charges and the scaled charges. The normal charges are point charges placed at the atom sites close to the quantum cluster with the formal charge values. The scaled charges are placed at the atom sites farther away from quantum cluster with charges scaled according to [46] to ensure fast convergence to the Madelung potential.

Projection embedding calculation

A smaller cluster, $Cu_2O_{11}La_4$, is selected out of the center of quantum cluster as WFT cluster (A) to host the correlation treatment (Fig. 1e). The cluster A consists of a Cu-O-Cu structure, along with its 6 peripheral oxygen, 4 apical oxygen and 4 shoulder lanthanum atoms (Fig. 1d). All Cu and O atoms within A are treated with cc-pVDZ basis set (Cu: 6s5p3d1f; O: 3s2p1d) [48, 49], while La atoms are treated with a 2s2p1d basis set selected out of ECP46MWB with ECP [50]. B layer atoms are treated with smaller basis sets where more core electrons are represented with ECP [51, 52], whose details can be found in SI. The entire basis set of A+B has 590 basis functions and 410 electrons (Fig. 4a step 1).

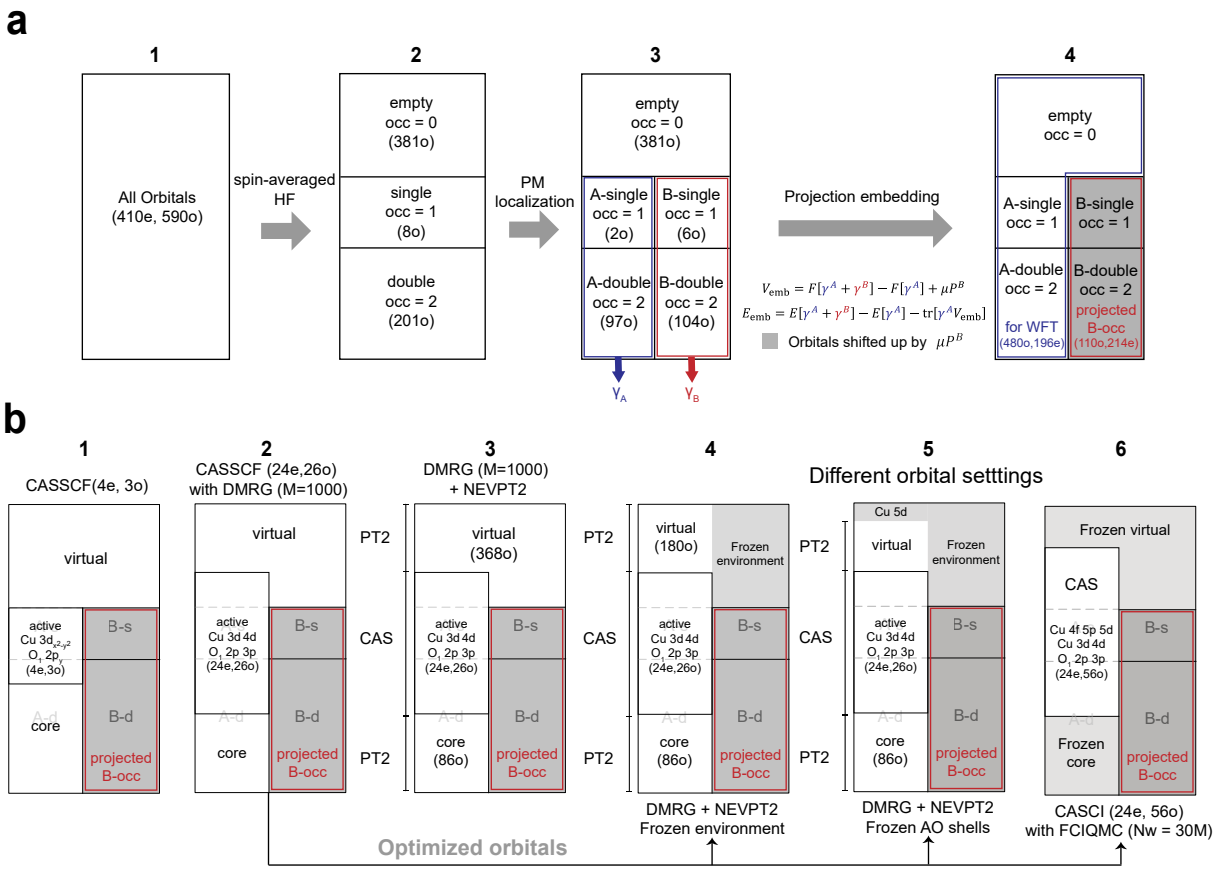

FIG. 4. Computational workflow and settings. (a) Quantum embedding scheme. A 3-layer spin-averaged Hartree-Fock calculation partitions the entire orbital space into 3 parts: empty, singly occupied and doubly occupied orbitals. Pipek-Mezey (PM) localization method is then used to partition singly and doubly occupied orbitals into those localized in region A (blue rectangle) and those localized in region B (red rectangle), from which RDMs of A and B (γ_A and γ_B) are obtained. γ_A and γ_B are then used to construct embedding potential V_{emb} and E_{emb}. B occupied orbitals are projected out of WFT calculation by shifting their energy by a large positive value μ, while the remaining orbital space (blue polygon) is considered for subsequent WFT calculations. (b) Correlated WFT calculations using CASSCF(4e,3o), DMRG+CASSCF(24e,26o), NEVPT2 and FCIQMC. Dark grey color with red boundary shows the projected occupied orbitals of region B. The "core", "active" and "virtual" denote the doubly occupied, correlated and empty orbitals, respectively. In NEVPT2 calculations, these terms mean perturbative core orbitals, multi-reference wave function space and perturbative virtual orbitals, respectively. Light grey shades indicate the frozen virtual/core orbitals in NEVPT2 and FCIQMC calculations.

The projection embedding scheme is followed to obtain an embedded Hamiltonian of A to describe its local electronic structure (Fig. 4a), similar to procedure in Ref [34]. The basic idea of projection embedding, in the case of WFT in HF, is to freeze the buffer wave function to the HF result. One starts from a converged HF solution for the whole quantum cluster (Fig. 4a step 2), partitions it into a direct product of cluster (A) and buffer (B), and then change A wave function to a correlated one, but leave B wave function unchanged. The freezing of B wave function is achieved in two steps: (1) by adding the Coulomb and exchange interaction between A and B into the external potential experienced by A, and (2) by increasing the energies of B-occupied orbitals by a large value, to effectively exclude those from subsequent calculations.

In cuprates, however, the ground state of parent compounds, even of a local cluster, is an antiferromagnetic state where spin-1/2 sites of A are entangled with those of B, such that A+B cannot be approximated by a product spin-adapted HF wave function. Therefore, in this work, a modified three-layer HF scheme, termed "spin-averaged HF", is used to obtain a spin-averaged open-shell environment for the cluster A, which preserves the direct product separability. In the following sub-sections, we will introduce the original projection embedding method, its spin-averaged HF variant, and the localization method in the presence of the spin-averaged HF.

Original projection embedding method

Let the quantum cluster HF wave function be $|\Psi^0\rangle$, and assume that it can be partitioned into a direct product

of A and B.

$$|\Psi^0\rangle = \hat{A}_0^\dagger \hat{B}_0^\dagger |\mathrm{vac}\rangle \tag{10}$$

The correlated methods are used to get a $\hat{A}^\dagger$ to describe A better. The embedded Hamiltonian is defined as

$$\langle \Psi_A^1 | \hat{H}_{\mathrm{emb}} | \Psi_A^2 \rangle = \langle \Psi_A^1 | \hat{B}_0 \hat{H} \hat{B}_0^\dagger | \Psi_A^2 \rangle \tag{11}$$

In this embedded Hamiltonian, the density matrix of B subsystem serves as a parameter, which is formulated as

$$(\rho_B^0)_{pq} = \langle \mathrm{vac} | \hat{B}_0 \hat{p}^\dagger \hat{q} \hat{B}_0^\dagger | \mathrm{vac} \rangle \tag{12}$$

Then the embedding Hamiltonian can be formulated as

$$\begin{aligned}
&\langle \Psi_A^1 | \hat{H}_{\mathrm{emb}} | \Psi_A^2 \rangle \\
&= \langle \Psi_A^1 | \hat{B}_0 \big[\hat{H}_A + \hat{H}_B \\
&+ \sum_{a_1 a_2 b_1 b_2} \big((a_1 a_2 | b_1 b_2) - (a_1 b_2 | b_1 a_2) \big) \hat{a}_1^\dagger \hat{b}_1^\dagger \hat{b}_2 \hat{a}_2 \big] \hat{B}_0^\dagger | \Psi_A^2 \rangle \\
&= \langle \Psi_A^1 | \big[\hat{H}_A + E_B^0 \\
&+ \sum_{a_1 a_2 b_1 b_2} \big((a_1 a_2 | b_1 b_2) - (a_1 b_2 | b_1 a_2) \big) \hat{a}_1^\dagger \hat{a}_2 (\rho_B^0)_{b_1 b_2} \big] | \Psi_A^2 \rangle
\end{aligned} \tag{13}$$

The 1-body embedding potential is

$$\begin{aligned}
\hat{V}_{\mathrm{emb}} &= \sum_{a_1 a_2 b_1 b_2} \big((a_1 a_2 | b_1 b_2) - (a_1 b_2 | b_1 a_2) \big) \hat{a}_1^\dagger \hat{a}_2 (\rho_B^0)_{b_1 b_2} \\
&= (F[\rho_A^0 + \rho_B^0] - F[\rho_A^0])_{a_1 a_2} \hat{a}_1^\dagger \hat{a}_2 .
\end{aligned} \tag{14}$$

The energy shift is

$$\begin{aligned}
E_{\mathrm{emb}} = E_B^0 &= E[\rho_A^0 + \rho_B^0] - E[\rho_A^0] \\
&- \sum_{a_1 a_2} (F[\rho_A^0 + \rho_B^0] - F[\rho_A^0])_{a_1 a_2} (\rho_A^0)_{a_1 a_2} .
\end{aligned} \tag{15}$$

$F[\cdot]$ and $E[\cdot]$ denote Fock matrix and energy functional of Hartree-Fock type, respectively. These additional terms are called embedding potential and energy correction, respectively. However, the embedding potential cannot restrict A wave function onto A orbitals, since B's occupied orbitals are still of low energy. Therefore, an energy shifting term ("projection term") is added to the embedding potential to raise the B occupied orbital energy to a prohibitively high level, forbidding A electrons to interact with them (Fig. 4a step 3 and 4).

$$\hat{P}_B = \mu \sum_b \hat{b}^\dagger \hat{b} \tag{16}$$

In this work, we set $\mu = 10^5 \mathrm{E_h}$.

In this way, we obtain the embedding potential $\hat{V}_{\mathrm{emb}} + \hat{P}_B$ and the energy correction $\hat{E}_{\mathrm{emb}}$, which describes the effect of environment B on A with B's density matrix as the only requirement.

Spin-averaged HF variant of projection embedding

In cuprates, the AFM ground state cannot be expressed with conventional RHF or ROHF wave functions, even approximately. In order to describe AFM environment at the mean-field level, we proposed a revised version of Hartree-Fock theory named spin-averaged HF to settle this problem. This procedure is similar to configuration-averaged Hartree–Fock (CAHF) [53, 54].

The spin-1/2 sites form AFM ground state, which can neither be separated into a direct product of A and B, nor expressed as a Slater determinant (SD), even in an approximate way. A direct localization of RHF orbitals requires ad-mixture between occupied and unoccupied orbitals, which changes the RDM. However, following smearing methods of SCF, we can define a Fock matrix with spinless fractional occupation.

$$F_{pq} = h_{pq} + \sum_r f_r \left((pq|rr) - \frac{1}{2}(pr|rq) \right), f_r = \begin{cases} 2, & r \in d; \\ 1, & r \in s; \\ 0, & r \in u. \end{cases} \tag{17}$$

where p, q and r denote spatial MOs, and f_r denote the occupation number of r, and d, s, u denote doubly-occupied, singly-occupied and empty orbitals, respectively (Fig. 4a step 2). In our system, the orbital occupation numbers are set according to the orbital energy order, and the number of Cu $3d_{x^2-y^2}$ open-shell orbitals of the system (Fig. 1d). SCF calculations can be done to diagonalize this Fock matrix, which yields a mean field approximation to the AFM ground state of the system, as well as a set of well-behaved orbitals as a starting point for further analysis. Since this HF method describes open-shell systems by considering the average effect of different spin configurations of environment, rather than a specific spin configuration, we dub this scheme "spin-averaged HF".

Localization method

d_A, d_B, s_A, s_B denote the intersection between doubly (singly) occupied orbitals and A (B) subsystem, and subsystem orbital set is defined by PM localization method (Fig. 4a step 3). This density matrix is then substituted into Eq (14) and Eq (15) to get the 1-body and 0-body embedding potential.

After delocalized spin-averaged HF orbitals are constructed, the (spin-traced) density matrix by mixed-HF is

$$(\rho^0)_{pq} = f_p \delta_{pq}, \tag{18}$$

Pipek-Mezey (PM) localization methods are used in doubly- (d) and singly-occupied (s) subspaces, respectively, to get localized orbitals without mixing orbitals of different occupation number. The subsystem partition of each local orbital is determined by the atom closest to

it. If the closest atom to an orbital is a $Cu_2O_{11}La_4$ (A) atom, then the orbital is labelled as A. If a $Cu_6O_{16}La_{12}$ (B) atom is the closest, then the orbital is labelled as B. Then the total spin-averaged HF density matrix is partitioned into subsystem A and B, defined as follows.

$$
\begin{aligned}
(\rho_A^0)_{pq} &= \begin{cases} 2\delta_{pq}, & p \in d \cap \mathrm{A}; \\ \delta_{pq}, & p \in s \cap \mathrm{A}; \\ 0, & p \in u \cup \mathrm{B}. \end{cases} \\
(\rho_B^0)_{pq} &= \begin{cases} 2\delta_{pq}, & p \in d \cap \mathrm{B}; \\ \delta_{pq}, & p \in s \cap \mathrm{B}; \\ 0, & p \in u \cup \mathrm{A}. \end{cases}
\end{aligned}
\tag{19}
$$

ρ_A^0 and ρ_B^0 is then substituted into Eq (14) and Eq (15) for the embedding potential (Fig. 4a step 4).

Correlated WFT calculations

After the embedding potential is obtained, different WFT calculations are conducted to calculate the correlation effects on the magnetic coupling J at different levels of approximation. The WFT calculation methods are illustrated in Fig. 4b, and described as follows.

CASSCF with DMRG as FCI solver (DMRG-CASSCF)

As the first step, CASSCF calculation on a small CAS (4e,3o) is performed with exact diagonalization FCI solver with `PySCF`[55, 56] (Fig. 4b step 1). The CAS consists of Cu $3d_{x^2-y^2}$ and bridging O $2p_\sigma$, and atomic valence active space (AVAS) [57] technique is used to generate the initial guess for orbital optimization. Then CASSCF on CAS(24e,26o) is performed with DMRG as the FCI solver. DMRG is performed using the `BLOCK2` package [17], with `PySCF` as the CASSCF driver[56] (Fig. 4b step 2). The DMRG calculation is performed with bond dimension $M = 1000$. The enlarged CAS includes the full Cu 3d space and bridging O 2p space, as well as higher-energy Cu 4d and bridging O 3p. In both CASSCF(4e,3o) and CASSCF(24e,26o), the singlet and triplet states are converged. The converged orbital set from CASSCF(24e,26o) is used in the subsequent steps.

Multi-reference perturbation (MRPT)

After DMRG-based orbital optimization, the effects of higher-energy orbitals are studied by correlating high-energy orbitals with the strongly contracted second-order n-electron valence state perturbation theory (SC-NEVPT2) with compressed perturber on the basis of DMRG (Fig. 4b step 3). [19, 20, 37] The NEVPT2 calculations can be split into three parts. First, the whole cluster space (blue polygon in Fig. 4a step 4) is included in PT space to calculate the dynamic correlation effect of all high-energy orbitals. Next, the environment empty orbitals are removed from PT space to calculate the environment effects (Fig. 4b step 4). Finally, multiple PT space settings are used to figure out the individual effects of each orbital shells (Fig. 4b step 5). Bond dimension $M = 1000$ and CAS(24e,26o) are used in all CAS and PT space settings. The atomic orbital shells in step 4 and 5 are defined by orthogonal projection of meta-Löwdin atomic orbitals [58] onto the core or virtual space, followed by a Gram-Schmidt orthogonalization to preserve the orbitals' similarity to meta-Löwdin AOs.

Full configuration interaction quantum Monte Carlo (FCIQMC)

In order to examine the accuracy of NEVPT2, FCIQMC calculations are performed and compared with NEVPT2 results on several small PT spaces (Fig. 4b step 6) [16, 36]. To improve convergence and reduce computational errors, we use the initiator approximation and adaptive shift methods throughout this work, with an initiator threshold $n_a = 3$ [59, 60]. We use a semi-stochastic approach with a deterministic space size of 1000 [61]. To obtain statistical average of energy, trial wave functions are constructed by diagonalizing the Hamiltonian within a subspace spanned by 10 most occupied SDs. In order to eliminate the initiator errors, we test FCIQMC with varying numbers of walkers, reaching up to 100 million walkers, such that the systematic error in energy is reduced to below 2 meV, which is very close to the typical statistic error in these systems. FCIQMC calculations on several typical active spaces involved in AFM J are performed to check their perturbation error. The FCIQMC results are presented in SI Section IV.

WFT evaluation of AFM coupling J

To compute AFM coupling J, we can follow the standard routine, where the energy spectrum of the embedded cluster (core layer A), containing 2 copper atoms, is mapped to a 2-site $S = 1/2$ nearest-neighbor Heisenberg model [38].

$$
\hat{H} = J\hat{\mathbf{S}}_1 \cdot \hat{\mathbf{S}}_2. \tag{20}
$$

In the AFM coupling case ($J > 0$), the ground state and the first excited state of the model above are the singlet and triplet states:

$$
\begin{aligned}
|\Psi_0\rangle &= \frac{1}{\sqrt{2}}(|\uparrow\downarrow\rangle - |\downarrow\uparrow\rangle), \quad E_0 = -\frac{3J}{4}; \\
|\Psi_1\rangle &= \frac{1}{\sqrt{2}}(|\uparrow\downarrow\rangle + |\downarrow\uparrow\rangle), \quad E_1 = \frac{J}{4}.
\end{aligned}
\tag{21}
$$

Therefore, the lowest-energy spin singlet and triplet states in *ab initio* calculation are mapped to $|\Psi_0\rangle$ and $|\Psi_1\rangle$ above, and J is calculated as the difference between corresponding energies. The spin-1/2 on each site

comes mainly from electrons occupying the open-shell Cu $3d_{x^2-y^2}$ orbitals. However, the many-body wave functions of low-energy states also include electron correlations from other high-energy orbitals, which significantly contribute to the magnetic coupling.

ACKNOWLEDGMENTS

This work was supported by the National Key R&D Program of China under Grant No. 2021YFA1400500, the Strategic Priority Research Program of the Chinese Academy of Sciences under Grant No. XDB33000000, the National Natural Science Foundation of China under Grant No. 12334003, and the Beijing Municipal Natural Science Foundation under Grant No. JQ22001. We are grateful for computational resources provided by the High Performance Computing Platform of Peking University.

[1] P. A. Lee, N. Nagaosa, and X.-G. Wen, Reviews of Modern Physics **78**, 17 (2006).
[2] N. Plakida, *High-Temperature Cuprate Superconductors: Experiment, Theory, and Applications*, Springer Series in Solid-State Sciences, Vol. 166 (Springer Berlin Heidelberg, Berlin, Heidelberg, 2010).
[3] X. Zhou, W.-S. Lee, M. Imada, N. Trivedi, P. Phillips, H.-Y. Kee, P. Törmä, and M. Eremets, Nature Reviews Physics **3**, 462 (2021).
[4] C. de Graaf and F. Illas, Phys. Rev. B **63**, 014404 (2000).
[5] J. P. Malrieu, R. Caballol, C. J. Calzado, C. de Graaf, and N. Guihéry, Chemical Reviews **114**, 429 (2014), pMID: 24102410.
[6] N. A. Bogdanov, G. Li Manni, S. Sharma, O. Gunnarsson, and A. Alavi, Nature Physics **18**, 190 (2022).
[7] Z.-H. Cui, H. Zhai, X. Zhang, and G. K.-L. Chan, Science **377**, 1192 (2022).
[8] V. M. Katukuri, N. A. Bogdanov, O. Weser, J. van den Brink, and A. Alavi, Physical Review B **102**, 241112 (2020).
[9] V. M. Katukuri, N. A. Bogdanov, and A. Alavi, Frontiers in Physics **10**, 836784 (2022).
[10] A. K. McMahan, R. M. Martin, and S. Satpathy, Physical Review B **38**, 6650 (1988).
[11] H. Das and T. Saha-Dasgupta, Physical Review B **79**, 134522 (2009).
[12] T. Jarlborg, Physical Review B **84**, 064506 (2011).
[13] C. Lane, J. W. Furness, I. G. Buda, Y. Zhang, R. S. Markiewicz, B. Barbiellini, J. Sun, and A. Bansil, Physical Review B **98**, 125140 (2018).
[14] L. Wang, G. He, Z. Yang, M. Garcia-Fernandez, A. Nag, K. Zhou, M. Minola, M. L. Tacon, B. Keimer, Y. Peng, and Y. Li, Nature Communications **13**, 3163 (2022).
[15] Q. Qin and Y.-f. Yang, npj Quantum Materials **10**, 13 (2025).
[16] K. Guther, R. J. Anderson, N. S. Blunt, N. A. Bogdanov, D. Cleland, N. Dattani, W. Dobrautz, K. Ghanem, P. Jeszenszki, N. Liebermann, G. L. Manni, A. Y. Lozovoi, H. Luo, D. Ma, F. Merz, C. Overy, M. Rampp, P. K. Samanta, L. R. Schwarz, J. J. Shepherd, S. D. Smart, E. Vitale, O. Weser, G. H. Booth, and A. Alavi, J. Chem. Phys. **153**, 034107 (2020).
[17] H. Zhai, H. R. Larsson, S. Lee, Z.-H. Cui, T. Zhu, C. Sun, L. Peng, R. Peng, K. Liao, J. Tölle, J. Yang, S. Li, and G. K.-L. Chan, J. Chem. Phys. **159**, 234801 (2023).
[18] S. Sharma and G. K.-L. Chan, J. Chem. Phys. **136**, 124121 (2012).
[19] C. Angeli, R. Cimiraglia, and J.-P. Malrieu, J. Chem. Phys. **117**, 9138 (2002).
[20] S. Guo, M. A. Watson, W. Hu, Q. Sun, and G. K.-L. Chan, J. Chem. Theory Comput. **12**, 1583 (2016).
[21] J. Miralles, O. Castell, R. Caballol, and J.-P. Malrieu, Chemical Physics **172**, 33 (1993).
[22] P. Pulay, International Journal of Quantum Chemistry **111**, 3273 (2011).
[23] J. Olsen, International Journal of Quantum Chemistry **111**, 3267 (2011).
[24] A. Van Oosten, R. Broer, and W. Nieuwpoort, Chemical Physics Letters **257**, 207 (1996).
[25] D. Muñoz, F. Illas, and I. de P. R. Moreira, Phys. Rev. Lett. **84**, 1579 (2000).
[26] C. J. Calzado and J.-P. Malrieu, Physical Review B **63**, 214520 (2001).
[27] L. Hozoi, M. S. Laad, and P. Fulde, Physical Review B **78**, 165107 (2008).
[28] K. Foyevtsova, J. T. Krogel, J. Kim, P. R. C. Kent, E. Dagotto, and F. A. Reboredo, Physical Review X **4**, 031003 (2014).
[29] L. K. Wagner and P. Abbamonte, Physical Review B **90**, 125129 (2014).
[30] Z.-H. Cui, J. Yang, J. Tölle, H.-Z. Ye, S. Yuan, H. Zhai, G. Park, R. Kim, X. Zhang, L. Lin, T. C. Berkelbach, and G. K.-L. Chan, Nature Communications **16**, 1845 (2025).
[31] F. C. Zhang and T. M. Rice, Physical Review B **37**, 3759 (1988).
[32] E. Pavarini, I. Dasgupta, T. Saha-Dasgupta, O. Jepsen, and O. K. Andersen, Physical Review Letters **87**, 047003 (2001).
[33] C. J. Calzado, J. F. Sanz, and J. P. Malrieu, J. Chem. Phys. **112**, 5158 (2000).
[34] F. R. Manby, M. Stella, J. D. Goodpaster, and T. F. I. Miller, J. Chem. Theory Comput. **8**, 2564 (2012).
[35] H. Werner and W. Meyer, J. Chem. Phys. **73**, 2342 (1980).
[36] G. H. Booth, A. J. W. Thom, and A. Alavi, J. Chem. Phys. **131**, 054106 (2009).
[37] A. Y. Sokolov, S. Guo, E. Ronca, and G. K.-L. Chan, J. Chem. Phys. **146**, 244102 (2017).
[38] C. de Graaf and R. Broer, *Magnetic Interactions in Molecules and Solids*, Theoretical Chemistry and Computational Modelling (Springer International Publishing, Cham, 2016).
[39] N. A. Bogdanov, R. Maurice, I. Rousochatzakis, J. van den Brink, and L. Hozoi, Phys. Rev. Lett. **110**, 127206 (2013).
[40] M. Pizzochero, R. Yadav, and O. V. Yazyev, 2D Materials **7**, 035005 (2020).
[41] T. Helgaker, P. Jørgensen, and J. Olsen, "The standard models," in *Molecular Electronic-Structure Theory* (John Wiley & Sons, Ltd, 2000) Chap. 5, pp. 142–200.
[42] L. Braicovich, L. J. P. Ament, V. Bisogni, F. Forte, C. Aruta, G. Balestrino, N. B. Brookes, G. M. De Luca, P. G. Medaglia, F. M. Granozio, M. Radovic, M. Salluzzo, J. van den Brink, and G. Ghiringhelli, Phys. Rev. Lett. **102**, 167401 (2009).
[43] R. Coldea, S. M. Hayden, G. Aeppli, T. G. Perring, C. D. Frost, T. E. Mason, S.-W. Cheong, and Z. Fisk, Phys. Rev. Lett. **86**, 5377 (2001).
[44] S. Gražulis, A. Daškevič, A. Merkys, D. Chateigner, L. Lutterotti, M. Quirós, N. R. Serebryanaya, P. Moeck, R. T.

Downs, and A. Le Bail, Nucleic Acids Research **40**, D420 (2012).
[45] B. Grande, H. Müller-Buschbaum, and M. Schweizer, Zeitschrift für anorganische und allgemeine Chemie **428**, 120 (1977).
[46] A. Gellé and M.-B. Lepetit, J. Chem. Phys. **128**, 244716 (2008).
[47] N. A. Bogdanov, "chargedel," (2021), Zenodo. https://doi.org/10.5281/zenodo.4444173.
[48] T. H. Dunning, J. Chem. Phys. **90**, 1007 (1989).
[49] N. B. Balabanov and K. A. Peterson, J. Chem. Phys. **125**, 074110 (2006).
[50] M. Dolg, H. Stoll, and H. Preuss, Theoretica chimica acta **85**, 441 (1993).
[51] M. M. Hurley, L. F. Pacios, P. A. Christiansen, R. B. Ross, and W. C. Ermler, J. Chem. Phys. **84**, 6840 (1986).
[52] R. B. Ross, J. M. Powers, T. Atashroo, W. C. Ermler, L. A. LaJohn, and P. A. Christiansen, J. Chem. Phys. **93**, 6654 (1990).
[53] R. McWeeny, Mol. Phys. **28**, 1273 (1974).
[54] M. C. Zerner, Int. J. Quantum Chem. **35**, 567 (1989).
[55] Q. Sun, J. Comp. Chem. **36**, 1664 (2015).
[56] Q. Sun, X. Zhang, S. Banerjee, P. Bao, M. Barbry, N. S. Blunt, N. A. Bogdanov, G. H. Booth, J. Chen, Z.-H. Cui, J. J. Eriksen, Y. Gao, S. Guo, J. Hermann, M. R. Hermes, K. Koh, P. Koval, S. Lehtola, Z. Li, J. Liu, N. Mardirossian, J. D. McClain, M. Motta, B. Mussard, H. Q. Pham, A. Pulkin, W. Purwanto, P. J. Robinson, E. Ronca, E. R. Sayfutyarova, M. Scheurer, H. F. Schurkus, J. E. T. Smith, C. Sun, S.-N. Sun, S. Upadhyay, L. K. Wagner, X. Wang, A. White, J. D. Whitfield, M. J. Williamson, S. Wouters, J. Yang, J. M. Yu, T. Zhu, T. C. Berkelbach, S. Sharma, A. Y. Sokolov, and G. K.-L. Chan, J. Chem. Phys. **153**, 024109 (2020).
[57] E. R. Sayfutyarova, Q. Sun, G. K.-L. Chan, and G. Knizia, J. Chem. Theory Comput. **13**, 4063 (2017).
[58] Q. Sun and G. K.-L. Chan, J. Chem. Theory Comput. **10**, 3784 (2014).
[59] D. Cleland, G. H. Booth, and A. Alavi, J. Chem. Phys. **132**, 041103 (2010).
[60] K. Ghanem, A. Y. Lozovoi, and A. Alavi, J. Chem. Phys. **151**, 224108 (2019).
[61] N. S. Blunt, S. D. Smart, J. A. F. Kersten, J. S. Spencer, G. H. Booth, and A. Alavi, J. Chem. Phys. **142**, 184107 (2015).